Mitigation of mode-one asymmetry in laser-direct-drive inertial confinement fusion implosions

O. M. Mannion, I. V. Igumenshchev, K. S. Anderson, R. Betti, E. M. Campbell, D. Cao, C. J. Forrest, M. Gatu Johnson, V. Yu. Glebov, V. N. Goncharov, V. Gopalaswamy, S. T. Ivancic, D. W. Jacobs-Perkins, A. Kalb, J. P. Knauer, J. Kwiatkowski, A. Lees, F. J. Marshall, M. Michalko, Z. L. Mohamed, D. Patel, H. G. Rinderknecht, R. C. Shah, C. Stoeckl, W. Theobald, K. M. Woo, and S. P. Regan

View Online   Export Citation   CrossMark

Physics of Plasmas
Features in **Plasma Physics Webinars**

Register Today!

Mitigation of mode-one asymmetry in laser-direct-drive inertial confinement fusion implosions

O. M. Mannion,[1,a] I. V. Igumenshchev,[1] K. S. Anderson,[1] R. Betti,[1] E. M. Campbell,[1] D. Cao,[1] C. J. Forrest,[1]
M. Gatu Johnson,[2] V. Yu. Glebov,[1] V. N. Goncharov,[1] V. Gopalaswamy,[1] S. T. Ivancic,[1] D. W. Jacobs-Perkins,[1]
A. Kalb,[1] J. P. Knauer,[1] J. Kwiatkowski,[1] A. Lees,[1] F. J. Marshall,[1] M. Michalko,[1] Z. L. Mohamed,[1] D. Patel,[1]
H. G. Rinderknecht,[1] R. C. Shah,[1] C. Stoeckl,[1] W. Theobald,[1] K. M. Woo,[1] and S. P. Regan[1]

AFFILIATIONS

[1]Laboratory for Laser Energetics, University of Rochester, Rochester, New York 14623, USA
[2]Massachusetts Institute of Technology, Plasma Science and Fusion Center, Cambridge, Massachusetts 02139, USA

Note: This paper is part of the Special Collection: Papers from the 62nd Annual Meeting of the APS Division of Plasma Physics.
[a]Author to whom correspondence should be addressed: omann@lle.rochester.edu

ABSTRACT

Nonuniformities present in the laser illumination and target in laser-driven inertial confinement fusion experiments lead to an asymmetric compression of the target, resulting in an inefficient conversion of shell kinetic energy to thermal energy of the hot-spot plasma. In this paper, the effects of asymmetric compression of cryogenic deuterium tritium laser-direct-drive implosions are examined using a suite of nuclear and x-ray diagnostics on the OMEGA laser. The neutron-averaged hot-spot velocity ($\vec{u}_{hs}$) and apparent ion temperature (T_i) asymmetry are determined from neutron time-of-flight measurements of the primary deuterium tritium fusion neutron energy spectrum, while the areal density (ρR) of the compressed fuel surrounding the hot spot is inferred from measurements of the scattered neutron energy spectrum. The low-mode perturbations of the hot-spot shape are characterized from x-ray self-emission images recorded along three quasi-orthogonal lines of sight. Implosions with significant mode-1 laser-drive asymmetries show large hot-spot velocities (>100 km/s) in a direction consistent with the hot-spot elongation observed in x-ray images, measured T_i asymmetry, and ρR asymmetry. Laser-drive corrections have been applied through shifting the initial target location in order to mitigate the observed asymmetry. With the asymmetry corrected, a more-symmetric hot spot is observed with reduced $\vec{u}_{hs}$, T_i asymmetry, ρR asymmetry, and a 30% increase in the fusion yield.

Published under license by AIP Publishing. https://doi.org/10.1063/5.0041554

I. INTRODUCTION

Laser-driven inertial confinement fusion (ICF)[1] experiments seek to produce an igniting plasma. A plasma is said to have ignited when the energy output from fusion reactions significantly exceeds that required to initially assemble the plasma.[2,3] To generate such a plasma, high-power lasers[4,5] are used to compress a spherical capsule filled with a deuterium tritium (DT) gas that is surrounded by a dense DT ice layer. As the laser irradiates the target, ablation of material from the outer surface of the capsule causes the target to implode radially inward, compressing and heating the DT gas to the ion temperatures (T_i) required for thermonuclear fusion to occur, while simultaneously compressing the DT fuel to the high areal densities (ρR) required to inertially confine the hot-spot plasma and ensure that the 3.5-MeV alpha particles generated from the DT fusion deposit their energy into the DT fuel.

To achieve an optimal conversion of initial laser energy to fusion output energy, a spherically symmetric implosion is required. In cryogenic DT ICF experiments performed at the National Ignition Facility (NIF)[4] and on the OMEGA laser,[5] perturbations exist in the laser and capsule that can cause asymmetric compression of the target. These perturbations are characterized by their Legendre-mode number $\ell = 2\pi R/\lambda$, where the perturbation wavelength λ is measured relative to the initial target radius R. These perturbations are categorized as either high mode (Legendre-mode number $\ell \geq 10$) or low mode ($\ell < 10$). High-mode perturbations can be generated from surface roughness of the DT ice layer, target mounts, laser imprint, or other small-scale features. Low-mode asymmetries can be generated by laser-drive nonuniformity due to power imbalance between beams, offset of the target relative to the laser drive, or laser beam mispointing, as well as large-scale defects within the target. High-mode asymmetries reduce the compressibility of the shell, reducing the shell areal density, and cause mixing of the cold DT fuel or ablator material into the hot spot, which act as a heat sink and extracts thermal energy from the

hot-spot plasma. Low-mode asymmetries lead to an asymmetric compression of the hot spot, poor confinement of the hot-spot plasma, and unconverted kinetic energy being present in the target near peak compression.

Previous work has shown that mode-one ($\ell = 1$) asymmetries present in either the radiation drive or the initial target uniformity can severely degrade the performance of ICF experiments.[6–9] When such asymmetries exist, they cause a pole-to-pole variation in the shell implosion velocity about the asymmetry axis. As the target implodes, the implosion velocity asymmetry causes the formation of a jet within the hot spot.[6] This jet undergoes a Helmholtz instability, which results in the formation of vortices within the hot spot. This motion within the hot spot represents residual kinetic energy (RKE) not used to heat and compress the target.[6] Additionally, when these asymmetries exist, the dense shell is formed asymmetrically around the hot spot and leads to poor confinement of the hot spot. The poor confinement and residual kinetic energy present in the target results in the fusion yield of the implosion being severely reduced.

To diagnose mode-one asymmetries in laser-direct-drive (LDD) implosions performed on the OMEGA laser, a suite of nuclear and x-ray diagnostics have been developed.[10–12] Neutron time-of-flight (nTOF) and charged-particle spectrometers are used to measure the neutron energy spectrum emitted from the target from which the fusion yield, hot-spot velocity, apparent ion temperature, and fuel areal density are inferred.[10,13–15] X-ray imaging diagnostics are used to measure the x-ray self-emission from the hot spot and are used to infer the size and shape of the hot spot.[11,16] These diagnostics have been fielded strategically around the OMEGA target chamber to provide a set of measurements of the hot spot and fuel conditions near peak compression which can be used to identify the presence of mode-one asymmetries.

In this paper, measurements made using the suite of nuclear and x-ray diagnostics on OMEGA are used to establish causal relationships between $\ell = 1$ asymmetries and implosion performance in LDD implosions on OMEGA. In particular, it will be shown that in implosions with large laser mode-one drive asymmetries, large hot-spot flow velocities (>100 km/s), ion temperature asymmetries ($\Delta T_i = 1.8$ keV), and areal-density asymmetries ($\Delta \rho R = 114$ mg/cm^2) are observed in the direction of the drive asymmetry and that the elongation observed in hot-spot x-ray self-emission images is also aligned with the measured hot-spot velocity direction. A mitigation strategy to eliminate laser mode-one drive asymmetries is then demonstrated, which uses the hot-spot velocity measurements and target offsets to apply laser-drive corrections. It will be shown that with the mitigation strategy applied, a more-symmetric hot spot and fuel distribution is obtained, and the fusion output is increased by 30%. Finally, the effect of mode-one asymmetries on the inferred hot-spot pressure is discussed for an ensemble of LDD implosions.

This paper is organized as follows: in Sec. II, the effects that laser mode-one drive asymmetries have on implosion performance are studied using 3D radiation-hydrodynamic simulations, and diagnostic signatures of these asymmetries are identified using synthetic neutron and x-ray diagnostics. In Sec. III, the suite of nuclear and x-ray diagnostics used on OMEGA to diagnose low-mode asymmetries are discussed. In Sec. IV, results from experiments with large laser-drive mode-one asymmetries are shown and Sec. V describes how these asymmetries have been mitigated. In Sec. VI, the effects that mode-

one asymmetries have on implosion performance are studied using an ensemble of recent LDD implosions on OMEGA. These results are summarized in Sec. VII.

II. EFFECT OF MODE-ONE ASYMMETRIES ON IMPLOSIONS

When the initial target mass areal density is uniform, mode-one drive asymmetries can result from an asymmetric ablation pressure of the form $P(\theta, \phi) = P_0 + \sum_{m=-1}^{m=1} c_1^m Y_1^m(\theta, \phi)$, where P_0 is the average ablation pressure, Y_1^m are the $\ell = 1$ spherical harmonic functions, and where c_1^m are the coefficients that describe the amplitude and direction of the ablation-pressure asymmetry. This ablation-pressure asymmetry can be caused by an asymmetric deposition of laser energy into the coronal plasma due to laser-energy imbalance, laser beam-pointing errors, laser–plasma interactions, or an initial target position offset.

Alternatively, when the ablation pressure is uniform, mode-one asymmetries present in the target can result from an asymmetric initial mass areal-density distribution in the target of the form $\rho R(\theta, \phi) = \rho R_0 + \sum_{m=-1}^{m=1} c_1^m Y_1^m(\theta, \phi)$, where ρR_0 is the average mass areal density, Y_1^m are the $\ell = 1$ spherical harmonic functions, and where c_1^m are the coefficients that describe the amplitude and direction of the mass areal-density asymmetry. This initial mass areal-density asymmetry can be caused by either density or thickness variations in the target which can be introduced by imperfections present during the formation of the DT ice layer or nonuniformities present in the ablator material.

In both cases, these asymmetries result in a pole-to-pole variation in the shell implosion velocity about the asymmetry axis which can be described using the expression $v_r(\theta, \phi) = v_0 + \sum_{m=-1}^{m=1} c_1^m Y_1^m(\theta, \phi)$, where v_0 is the average implosion velocity, Y_1^m are the $\ell = 1$ spherical harmonic functions, and where c_1^m are the coefficients that describe the amplitude of the asymmetry. Such asymmetries have been studied in laser indirect drive (LID) implosions on the NIF and have been shown to severely degrade implosion performance.[8,9]

To study the effects that laser mode-one drive asymmetries have on LDD implosions in more detail, a set of simulations were performed using the 3D radiation-hydrodynamic code *ASTER*.[17,18] In these simulations, a laser mode-one drive asymmetry of varying strength was introduced by altering the energy balance of the 60 laser beams used to drive the target. These simulations used the laser pulse and target design for OMEGA shot 94712 (see Fig. 1) and the direction of the laser mode-one drive asymmetry was chosen to match the direction of the hot-spot velocity measured in this experiment (see Sec. IV). These simulations also included the asymmetry introduced by the OMEGA beam-port geometry and used the as shot laser pulse.

An example of the target mass-density profile at peak neutron production from one of the *ASTER* simulations is shown in Fig. 2. We see that near peak neutron production a jet in the central hot-spot region has been formed and travels in the direction of the drive asymmetry. The shear flow along the sides of the jet causes a Helmholtz instability, which results in the formation of vortices in the hot spot. At peak compression, there is an asymmetric distribution of the DT fuel around the hot spot, which results in poor confinement of the hot-spot plasma, and eventually the jet material punctures the low-density fuel region. The large flow velocities present in the hot spot represent RKE in the target that did not contribute to generating fusion reactions.
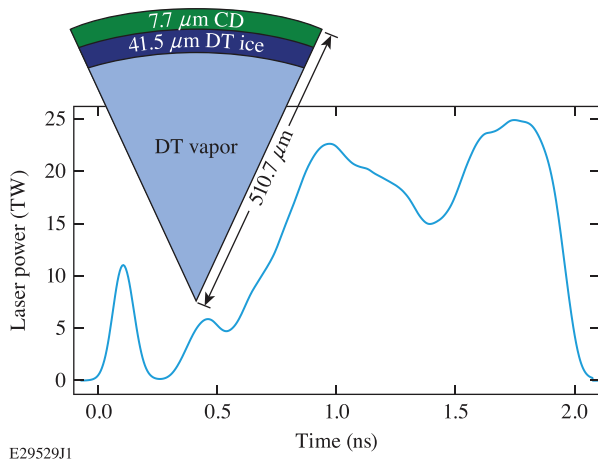
FIG. 1. The laser pulse and target design for OMEGA shot 94712.

FIG. 2. The equatorial mass-density profile of a target at peak neutron production from the 3D radiation-hydrodynamic code *ASTER* when a laser mode-one drive asymmetry was introduced. The flow velocity field within the hot-spot region is shown as the white arrows. The directions along which the synthetic neutron energy spectrum and x-ray images are calculated (see Figs. 4 and 5) are indicated by the dashed lines.

FIG. 3. The simulated fusion yield (blue curve) and residual kinetic energy fraction (orange curve) from a series of 3D *ASTER* simulations where a laser illumination mode-one drive asymmetry of varying strength was introduced.

The poor confinement and RKE caused by the mode-one drive asymmetry results in the fusion yield being reduced with respect to 1D predictions. This can be seen in Fig. 3, which shows the fusion yield and residual kinetic energy fraction as a function of the laser mode-one drive asymmetry amplitude $\sigma_{rms}^{\ell=1}$ for the series of *ASTER* simulations that were performed. To calculate the laser mode-one drive asymmetry amplitude $\sigma_{rms}^{\ell=1}$, a spherical harmonic decomposition of the laser illumination nonuniformity determined by a hard sphere calculation was performed. Here we have defined the residual kinetic energy fraction as
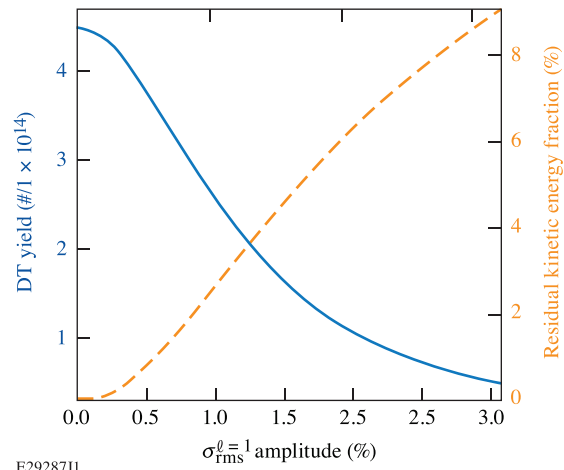
$$\text{RKE} = \frac{\min[\text{KE}_{3D}(t)] - \min[\text{KE}_{1D}(t)]}{\max[\text{KE}_{1D}(t)]}, \quad (1)$$

where $\min[\text{KE}_{3D}(t)]$ and $\min[\text{KE}_{1D}(t)]$ are the minimum kinetic energy achieved after the start of the deceleration phase in the 3D and 1D *ASTER* simulations, respectively, and $\max[\text{KE}_{1D}(t)]$ is the maximum kinetic energy obtained in the 1D simulation. From Fig. 3, we see that as the laser mode-one drive asymmetry increases, the fusion yield decreases while the RKE increases. It should be noted that there are several definitions of RKE in the literature.[7,19] Here, we have chosen this definition of RKE as it captures the excess kinetic energy due to 3D effects and eliminates the impact of 1D residual kinetic energy.

To study the effects that mode-one drive asymmetries have on the neutron energy spectrum emitted from an ICF implosion, the *ASTER* simulation shown in Fig. 2 was post-processed using the Monte Carlo neutron transport code *IRIS3D*.[22] In these calculations, DT and deuterium-deuterium (DD) neutrons are generated in the hot spot with a neutron energy spectrum given by the local temperature, density, and velocity.[23,24] These neutrons are then transported through the target to the detector, elastically scattering off the D and T in the fuel by an amount proportional to the areal density experienced along the neutron transport path and the scattering cross section. These calculations were performed at 10 ps intervals over the ~100 ps burn width.

Figure 4 shows the time-integrated neutron energy spectrum calculated along the three directions shown in Fig. 2. The large peaks in the neutron energy spectrum at 14.028 and 2.45 MeV are the primary DT and DD fusion neutrons, respectively. The broad spectral features between 1.5 and 13 MeV are primary DT fusion neutrons that have elastically scattered off the D and T in the fuel. The sharp edge features at 1.5 and 3.5 MeV are the nT and nD elastic backscatter edges.[25] In these calculations, only the D(n,n')D' and T(n,n')T' elastic scattering reactions were considered. The effect that other scattering reactions such as the D(n,2n)p reaction have on the neutron energy spectrum is an area of active research[26,27] but is expected to be a second order effect at the areal densities achieved at OMEGA.
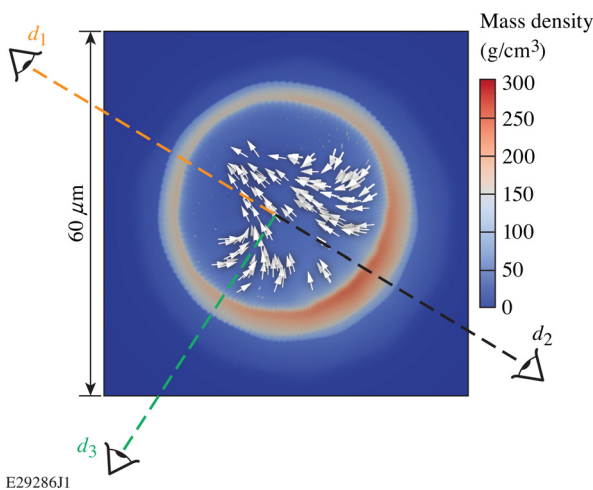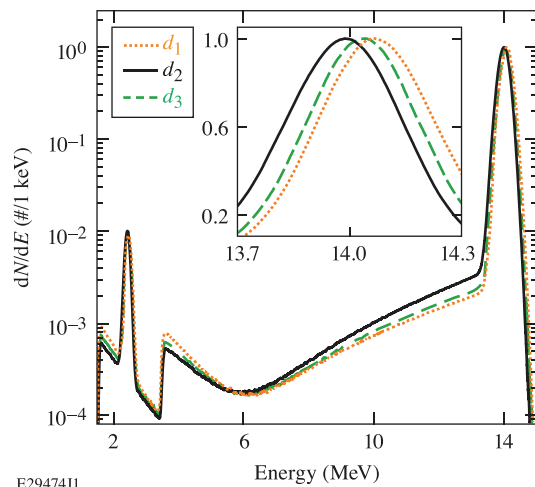
FIG. 4. The synthetic neutron energy spectra calculated by post-processing the 3D *ASTER* results shown in Fig. 2, with the neutron transport code *IRIS3D*. The spectra are shown for a detector along (orange curves), orthogonal (green curves), and opposite (black curves) the mode-one drive asymmetry direction (see Fig. 2). The inset shows the calculated primary DT neutron energy spectrum on an expanded scale. For simplicity, these calculations have included only primary DT and DD fusion reactions, and single elastic nD and nT scattering events.

The primary DT neutron energy spectrum is shown in the inset of Fig. 4 and highlights how the mean energy of the neutron energy spectrum varies along each measurement direction. We see that the neutron energy spectrum measured by a detector along the direction of the hot-spot velocity, such as d_1, has a mean energy higher than the nominal mean energy of DT neutrons, while the spectrum measured by a detector opposite the hot-spot velocity, such as d_2, has a mean energy lower than the nominal mean energy of DT neutrons, and the spectrum measured by a detector orthogonal to the hot-spot velocity, such as d_3, has the nominal mean energy of DT neutrons. Previous work has shown that the mean energy of the primary fusion neutron energy spectrum is the sum of a thermal and nonthermal component.[28,29] The thermal component is isotropic along all diagnostic lines of sight and is referred to as the Gamow shift.[10,28] The nonthermal term originates from the Doppler shift introduced to the neutrons as a result of the velocity of the hot spot, and is responsible for the peak shifts observed in Fig. 4. Therefore, measurements of the mean energy of the primary neutron energy spectrum can be used to infer the hot-spot velocity present in an implosion.

Calculations of the variance of the primary DT neutron energy spectra shown in Fig. 4 also reveal an anisotropy along the different lines of sight. In particular, the standard deviations of the primary DT peaks measured along the directions d_1 and d_2 were both 166 keV, while the standard deviation of the peak along d_3 was 158 keV. It has been shown that the variance of the primary fusion neutron energy spectrum is the sum of a thermal and nonthermal component.[24,29,30] The thermal component is isotropic and is proportional to the thermal ion temperature of the hot spot. The nonthermal term is proportional to the flow velocity variance along the measurement line of sight (LOS)[7] and causes the variances of the primary fusion peaks to be different along each line of sight. Note that because the velocity-variance calculation is identical along opposing lines of sight, opposing lines of sight such as d_1 and d_2 will measure identical variances in the neutron energy spectrum. In ICF experiments, the variance of the primary neutron energy spectrum is typically used to infer the apparent ion temperature of the experiment. Therefore, measurements of the apparent ion temperature asymmetries can be used to infer the flow velocity variances within the hot spot.[7]

Figure 4 also shows that the scattered neutron energy spectra are different along each measurement direction. To understand the trends in the scattered neutron energy spectra, we first note that these neutrons have been generated in the hot-spot region and have elastically scattered off the D and T present in the dense fuel as they exit the target. The energy at which a neutron exits the scattering reaction is directly related to the neutron scattering angle, and is therefore associated with scattering in a particular region of the capsule.[31] Additionally, the number of scattered neutrons is proportional to the areal density along the neutron path length. As a consequence of these two factors, the number of scattered neutrons in different regions of the neutron energy spectrum is proportional to the areal density in different regions of the target.[26] For example, neutrons that have elastically scattered off the T in the dense fuel layer and exited the reaction at energies between 9 and 11 MeV have undergone a forward scatter event and therefore have originated from the region of the capsule along the detector line of sight. Conversely, neutrons that elastically scatter off T in the dense fuel and exited the reaction at energies between 3.5 and 4.0 MeV have undergone a backscatter event, and therefore have originated from the region of the capsule opposite the detector line of sight.

Therefore, the trend in the scattered neutron energy spectrum shown in Fig. 4 is due to the areal-density asymmetries of the target. In particular, we see that the neutron energy spectrum measured along d_1, which is directed along a low areal-density region of the target (see Fig. 2), has the lowest number of scattered neutrons in 9–11 MeV region, while the neutron energy spectrum measured along d_2, which is directed along a high areal-density region of the target (see Fig. 2), has the highest number of scattered neutrons in the 9–11 MeV region. Conversely, we see the opposite trend is true near the 3.5–4.0 MeV region of the neutron energy spectrum as these neutrons are sampling the region of the target opposite the detector directions. Therefore, by measuring the neutron energy spectrum along different lines of sight, the areal-density asymmetry of the target can be inferred.

To study the effects that mode-one drive asymmetries have on different x-ray imaging diagnostic measurements, the *ASTER* simulation shown in Fig. 2 was post-processed to generate x-ray self-emission images along different lines of sight. For this calculation, the x-ray emission in the hot spot was calculated using the local density and temperature conditions, and the x rays were then transported to each detector plane assuming an optically thin plasma.

Figure 5 shows the synthetic x-ray self-emission images as simulated for a detector near on axis and near orthogonal to the mode-one perturbation. These images have accounted for the photon sensitivity of the x-ray imagers on OMEGA (see Sec. IV), which are peaked in the 4 to 9 keV photon energy range. A 6-μm point-spread function has been applied to the images. The images are either time resolved [Fig. 5(a)] with a 15 ps time resolution or time integrated [Fig. 5(b)]. The hot-spot flow velocity from the simulation has been projected into each detector plane and is shown for reference.
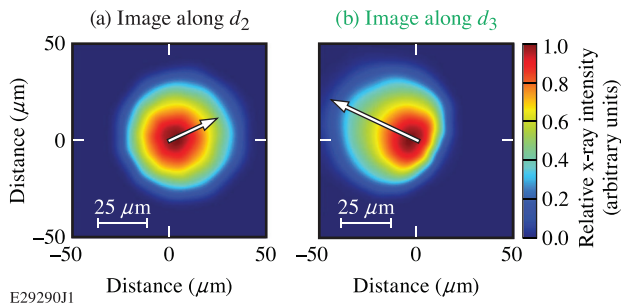
FIG. 5. The synthetic x-ray images observed from a detector (a) near on axis and (b) near orthogonal to the mode-one direction (see Fig. 2). The projection of the hot-spot velocity into the detector plane is indicated by the white arrow. The magnitude of the projection is indicated by the length of the white arrow.

FIG. 6. A sinusoidal projection of the OMEGA target chamber with the different diagnostic ports labeled. Lines of sight that measure hot-spot velocities are red, apparent ion temperature LOS are orange, areal-density LOS are blue, and x-ray imaging LOS are green. The direction along which the target stalk is located is shown in gray. Multiple quantities are diagnosed along some of the lines of sight.

The asymmetry observed in the synthetic x-ray images depends on the viewing direction of the detector with respect to the asymmetry direction. If the x-ray image is taken along the direction of the laser mode-one drive asymmetry, as is the case for detector d_2, little distortion to the hot-spot x-ray image is observed [see Fig. 5(a)]. If the x-ray image is taken nearly orthogonal to the direction of the laser-drive asymmetry, as is the case for detector d_3, a large distortion to the hot-spot x-ray image is observed [see Fig. 5(b)]. Additionally, the asymmetry observed in these images is along the projection of the hot-spot velocity into the detector plane, and the magnitude of the asymmetry is proportional to the hot-spot velocity.

It should be noted that the laser mode-one drive asymmetry used in these simulations are only an approximation of the laser mode-one drive asymmetry that was present on shot 94712. As mentioned previously, the mode-one drive asymmetry in these simulations was introduced through laser-energy imbalance, while in the experiment the laser mode-one asymmetry was due to large laser beam-pointing errors (see Sec. IV). In order to accurately model drive asymmetries caused by large laser beam-pointing errors, a full 3D cross-beam energy transfer (CBET) ray trace laser-energy deposition model[20] is required, and is not currently available in *ASTER*. Recent work[21] using a full 3D CBET ray trace laser-energy deposition model has shown that CBET effects can reduce mode-one drive asymmetries, and so the *ASTER* results shown here likely overestimate the effect of mode-one asymmetries. Although using the approximate drive asymmetry in these simulations prevents a direct comparison of these results with the experimental data, they are still useful in developing an understanding of the effect that laser mode-one drive asymmetries have on LDD implosion performance and identifying the diagnostic signatures of such asymmetries.

III. THREE-DIMENSIONAL NUCLEAR AND X-RAY DIAGNOSTICS ON OMEGA

Mode-one asymmetries present in the initial target fabrication or in the laser drive are diagnosed using a suite of nuclear and x-ray diagnostics on OMEGA. These detectors have been placed strategically around the OMEGA target chamber to provide quasi-orthogonal measurements of the neutron energy spectrum and x-ray self-emission emitted from the target. Figure 6 shows the different lines of sight on OMEGA and the diagnostic measurements made along each line of sight.
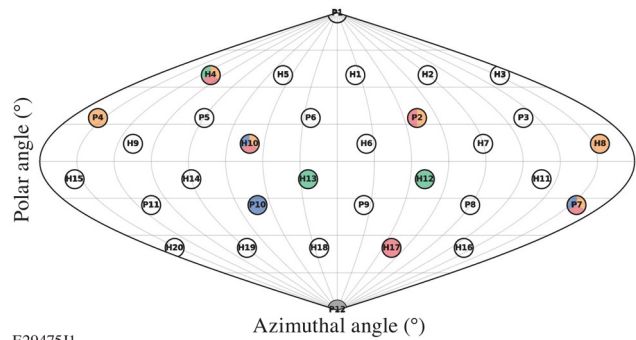
Measurements of the neutron energy spectrum are obtained using nTOF spectrometers[32] and a magnetic recoil spectrometer (MRS).[33] The primary DT fusion neutron energy spectrum is used to directly measure the fusion yield, apparent ion temperature, and the Doppler shift along the measured LOS. The scattered neutron energy spectrum is used to infer the areal density using a point source single scatter model, which converts the number of scattered neutrons in a particular region of the spectrum, into an areal density.[34]

It is important to note that the values inferred from the primary fusion neutron energy spectrum are neutron-averaged quantities[35] while the areal densities inferred from the scattered neutron energy spectrum are neutron path-integrated quantities.[26] Additionally, as discussed in Sec. II, depending on the region of the neutron energy spectrum measured, the areal density can be inferred in different regions of the target. Neutron time-of-flight detectors on OMEGA infer the areal density from the 3.5 to 4-MeV region of the scattered neutron energy spectrum.[14] This corresponds to neutrons with an average scattering cosine of $\mu = -0.9$ (i.e., back-scattered neutrons). Consequentially, the nTOF detectors on OMEGA sample the areal density in the region of the fuel opposite of the detector LOS since the neutrons being measured have interacted with the region of the shell opposite the LOS, back scattered, and then arrived at the detector.[31] The MRS detector on OMEGA infers the areal density from the 9 to 11-MeV region of the scattered neutron energy spectrum, which corresponds to neutrons with an average scattering cosine of $\mu = 0.7$ (i.e., forward-scattered neutrons). Consequentially, the MRS detector on OMEGA samples the region of the fuel along the detector LOS.[26,31]

There are seven nTOF LOS on OMEGA that measure the DT primary neutron energy spectrum. Six of these LOS have detectors that are positioned sufficiently far from the target chamber center (TCC) to enable the apparent ion temperature along the LOS to be measured with an accuracy of ~ 250 eV.[36] Five of these LOS have nTOF detectors that are equipped with timing fiducials that enable an absolute time-of-flight measurement[37] to be made from which the Doppler shift in the neutron mean energy can be inferred, which is then used to determine the hot-spot velocity along the detector LOS.[10,13,38,39] There are three detectors on OMEGA that measure the scattered neutron energy spectrum, two of which are nTOF detectors

that measure the nT backscatter edge[14,40] and one MRS detector that measures the forward-scattered neutron energy spectrum.

Measurements of the hot-spot x-ray self-emission images on OMEGA are made using two time-resolved imagers and one time-integrated x-ray imager.[11,12] These diagnostics have a spatial resolution of ~6 μm and the time-resolved diagnostics have a time resolution of 15 to 40 ps. The x-ray imaging diagnostics are sensitive to x-rays having photon energies in the 4 to 9 keV range. These detectors are positioned along three quasi-orthogonal lines of sight and are shown in Fig. 6.

IV. MEASUREMENTS OF MODE-ONE ASYMMETRIES

Large mode-one drive asymmetries have been observed when abnormally large errors in the laser alignment exist. To align all 60 OMEGA beams to TCC, a two-step process is performed. First, a ~860 μm diameter glass sphere with a reflective aluminum oxide coating is placed at TCC and a low-energy UV alignment beam is propagated through each beamline. Adjustments are made to the beam alignment mirrors until each beam is retroreflected off the sphere at TCC to verify the beam alignment. This process is referred to as laser targeting and provides initial alignment of the laser beams to TCC. The second step in aligning the system is referred to as laser beam pointing and provides precise alignment ($\sigma_{rms} \sim 10$ μm with worst beam <20 μm out of alignment) of the laser beam pointing. During laser beam pointing, a 4-mm diameter Au sphere is placed at TCC using a high-speed video camera and all 60 OMEGA laser beams illuminate the Au sphere using the full laser energy. X rays are generated at the locations where the beams hit the Au sphere and these x rays are measured using x-ray pinhole cameras.[41,42] An example of the laser beam-pointing data taken with the x-ray pinhole cameras on a typical pointing shot on OMEGA is shown in Fig. 7(a). The position of each beam is determined by fitting the measured beam profile seen by the x-ray pinhole cameras with a super-Gaussian profile. Any deviation from the ideal laser beam-pointing configuration[5] is determined, and appropriate modifications to the laser beam positioning are made. This two-step alignment process is typically capable of positioning each of the 60 beams on OMEGA to their desired location with $\sigma_{rms} < 10$ μm.

Errors can occur in the laser beam-pointing procedure if target defects exist on the spheres used for beam targeting and beam pointing. For OMEGA shots 94657, 94660, 94712, and 94715, the aluminum oxide coating on the target used during the laser targeting had unintentional coating defects, which caused gross mispointing of the laser beams to be introduced during the targeting procedure. Additionally, the Au spheres used during the laser pointing procedure for these experiments had unintentional nonuniform Au coatings as a result of target fabrication issues. The nonuniform Au coating resulted in weak x-ray signals being generated by specific beams as shown in Fig. 7(b). The weak signals led to large uncertainties in identifying the position of these beams and resulted in large beam-pointing errors being introduced during the beam-pointing procedure. The compounding errors in the alignment of the laser system during these experiments resulted in a large laser mode-one asymmetry being present.

Figure 8 shows the laser illumination perturbation on target for shot 94712. The laser illumination on target was determined from a hard sphere calculation, which determines the overlap intensity of all 60 beams on the initial target radius, accounting for the laser beam pointing, laser beam energy, and target offset.[41] The laser beam pointing was determined during the beam alignment procedure described above, the laser beam energy was measured using a calorimeter, and the target offset was measured by both a high-speed video camera and x-ray pinhole cameras.[43] Including all known effects, the total illumination nonuniformity was found to be 27.3%.

Both the target offset, and the laser-energy imbalance were small for this shot, and so did not contribute significantly to the asymmetry observed in Fig. 8. To confirm this, the hard sphere calculations were repeated including each effect (pointing, target offset, beam energy balance) separately. When the laser-energy balance and target positioning were assumed perfect, but the measured laser pointing was included, the total illumination nonuniformity was found to be 29.0%. When the laser-energy balance was assumed perfect, but the measured laser pointing and small <5 μm target offset was included, the total
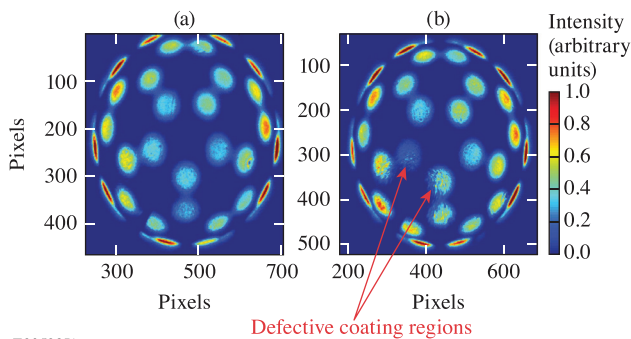

E29528J1

FIG. 7. X-ray pinhole camera measurements of the OMEGA beam pointing from (a) a typical OMEGA campaign when the Au coating of the pointing target is uniform and (b) measurements when the Au coating has large defects as was the case during the pointing shots used to align the laser prior to the shots discussed in Secs. IV and V.
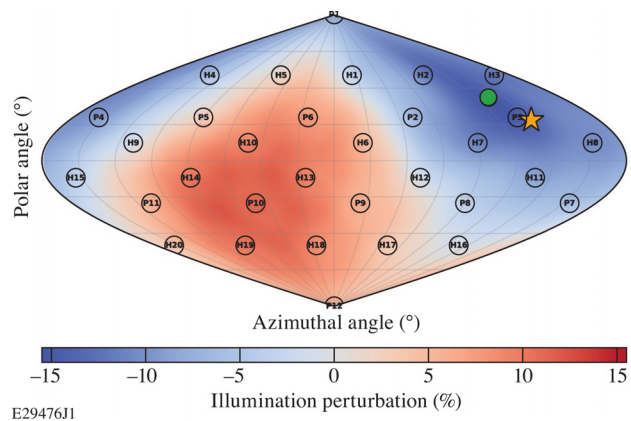

E29476J1

FIG. 8. A sinusoidal projection of the OMEGA target chamber showing the illumination perturbation for shot 94712 determined from a hard sphere calculation which used the measured laser beam pointing, energy, and target offset. The direction of the measured hot-spot velocity is shown as the orange star and had a magnitude of 146 ± 12 km/s. The laser mode-one illumination asymmetry $\sigma_{rms}^{\ell=1}$ amplitude was 7.3% and the direction is shown as the green circle.

illumination nonuniformity was found to be 27.9%. When the target positioning was assumed perfect, but the measured laser pointing and laser energies were included, the total illumination nonuniformity was found to be 28.6%. Therefore, we can conclude that the asymmetry observed in Fig. 8 originated from the laser beam-pointing errors.

The calculated on-target illumination perturbation for shot 94712 shows that a large mode-one drive asymmetry was present with a total variation of 27.3% across the target. Figure 9 shows the Legendre-mode spectral decomposition for the laser illumination perturbation shown in Fig. 8. The laser mode-one illumination asymmetry $\sigma_{rms}^{\ell=1}$ amplitude was 7.3% and was oriented along $\theta = 51°$ and $\phi = 122°$ as shown in Fig. 8. Note that we are using a convention in which the mode-one direction is taken to be along the drive deficit to aid in the comparison with the hot-spot velocity measurement direction.

Measurements made using the nuclear and x-ray diagnostics on OMEGA were able to identify the presence of the laser mode-one drive asymmetry. In particular, a hot-spot velocity of 146 ± 12 km/s was inferred from the nTOF's in the direction of $\theta = 64° \pm 7°$ and $\phi = 133° \pm 4°$. The apparent ion temperature asymmetry was 1.8 ± 0.5 keV as measured from the nTOF detectors. The highest apparent ion temperature was 5.9 ± 0.2 keV as measured along the H8 LOS and the minimum apparent ion temperature was 4.1 ± 0.2 keV as measured along the P2 LOS. Finally, the areal-density asymmetry was 104 ± 18 mg/cm^2 as inferred from the nTOF and MRS detectors. The lowest inferred areal density was measured from the H10 nTOF detector, which measures the areal density along the H11 LOS, while the highest areal density was inferred from the MRS detector, which measures the areal density near the P10 LOS.

The direction of the hot-spot velocity was found to be consistent with the direction of the initial laser-drive mode-one asymmetry. This can be seen in Fig. 8, which shows that the hot-spot velocity was measured along the direction of the laser mode-one drive asymmetry. The
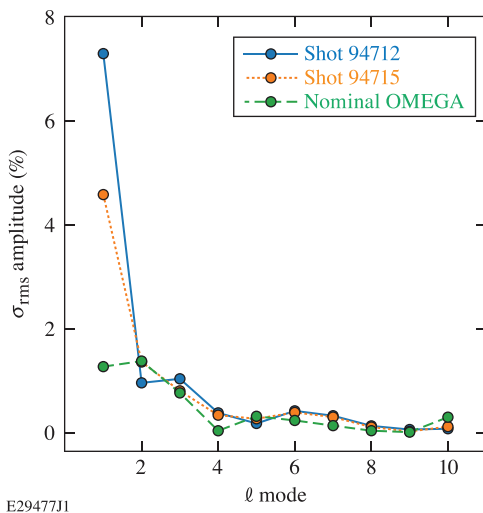
slight discrepancy between the direction of the laser mode-one drive asymmetry and the hot-spot velocity is within the directional uncertainty in the hot-spot velocity measurement.[44]

To facilitate comparison between the apparent ion temperature measurements with the direction of the laser-drive asymmetry, Fig. 10 shows the apparent ion temperature measurements plotted as a function of the projection of the hot-spot velocity $\vec{u}_{hs}$ along the measurement direction $\hat{d}_i$. We see that the highest apparent ion temperatures were observed along and opposite to the direction of the hot-spot velocity, while the lowest apparent ion temperature was observed near orthogonal to the hot-spot velocity. This is consistent with a jet being formed in the hot-spot region that generates vortices along the direction of the mode-one, causing variations in the flow velocity within the hot spot. A fit to the apparent ion temperatures is shown in Fig. 10 using the expression[6] $(T_i)_j = T_0 + \Delta T \zeta_j^2$, where $\zeta_j = \hat{u}_{hs} \cdot \hat{d}_j$. The values inferred from the fit are $T_0 = 4.3$ keV and $\Delta T = 2.2$ keV.

To facilitate comparison between the inferred areal densities and the direction of the laser-drive asymmetry, Fig. 11 shows the areal-density measurements plotted as a function of the projection of the hot-spot velocity along the measurement line of sight, corrected for the average neutron scattering cosine μ_i of each measurement. Note that the μ_i correction is required to make a direct comparison between data taken for the nTOF and MRS measurements. From Fig. 11, we see that the highest areal density is observed in the direction opposite of the hot-spot velocity direction, while the lowest areal density is observed along the hot-spot velocity direction. This correlation between the hot-spot velocity and areal-density asymmetry has previously been observed in LID implosions on the NIF.[8] A fit to the inferred areal-density measurements is shown in Fig. 11 using the expression $(\rho R)_i = \rho R_0 + \Delta \rho R \eta_i$, where $\eta_i = \hat{u}_{hs} \cdot \hat{d}_i \mu_i$. The values inferred from the fit are $\rho R_0 = 116$ mg/cm^2 and $\Delta \rho R = -55$ mg/cm^2.

These measurements were also consistent with the asymmetry observed in the measured hot-spot x-ray self-emission images.

FIG. 9. A Legendre-mode spectral decomposition of the laser illumination perturbations shown for shots 94712 (blue curve, see Fig. 8) and 94715 (orange curve, see Fig. 13) and a nominal OMEGA shot (green curve). The nominal OMEGA curve is taken from a shot which represents the typical illumination uniformity achieved on OMEGA when no gross beam-pointing errors or target offsets are present.
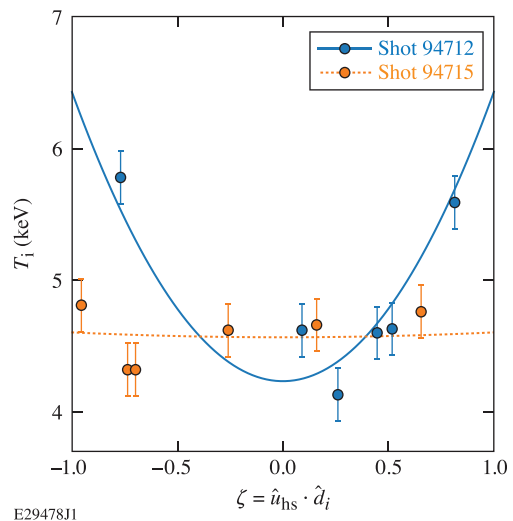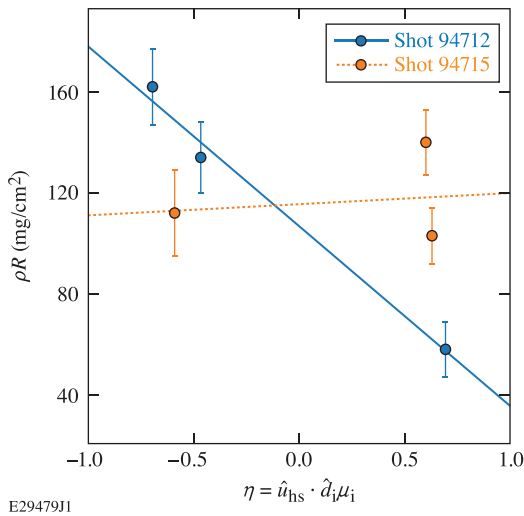

FIG. 10. The apparent ion temperature measurements for shots 94712 (blue) and 94715 (orange) as a function of the projection of the detector direction with the measured hot-spot velocity direction. The solid curves are fits to the data using the functional form $T_i = T_0 + \Delta T \zeta^2$.

FIG. 11. The inferred areal-density measurements for shots 94712 (blue) and 94715 (orange) as a function of the projection of the detector direction with the measured hot-spot velocity direction, modified by the average scattering cosine μ_i of the measurement. The solid curves are fits to the data using the functional form $\rho R = \rho R_0 + \Delta\rho R\eta$.

Figure 12 shows the x-ray self-emission images measured on shot 94712 by the three x-ray diagnostic imagers on OMEGA. The measured hot-spot velocity has been projected into each detector plane and is shown as the white vector. The elongation observed in the hot-spot x-ray images is consistent with the direction of the hot-spot flow velocity. It is important to note that the x-ray image shown in Fig. 12(b) was measured along the H13 LOS, which is on axis of the mode-one drive asymmetry (see Fig. 8) and so is not expected to observe the drive asymmetry [see Fig. 5(a)]. A quantitative analysis of these x-ray measurements is being developed and will be the focus of future work.

V. MITIGATION OF MODE-ONE ASYMMETRIES

The experimental results highlighted in Sec. IV for shot 94712 were reproduced on shots 94657 and 94660. Each of these experiments
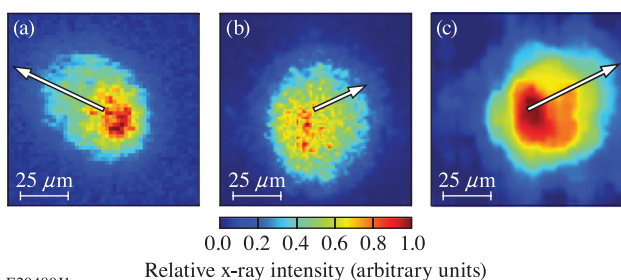
FIG. 12. The x-ray self-emission images measured for shot 94712. The (a) single-line-of-sight, time-resolved x-ray imager (SLOS-TRIXI)[12] and (b) KB framed[11] images are time resolved and are averaged over a 40 and 15 ps time window around peak neutron production, respectively, while the (c) gated monochromatic x-ray microscope (GMXI)[11] image is time integrated. Each detector has a ~6 μm spatial resolution. The projection of the measured hot-spot velocity into the detector plane is indicated by the white arrow. The magnitude of the projection is indicated by the length of the white arrow.

used nearly identical laser pulses and target dimensions as shot 94712 (see Fig. 1). The nuclear and x-ray measurements on each of these experiments were consistent with the asymmetry observed in 94712, and the fusion yield was significantly lower than expectation. Based on these observations, an effort was undertaken to mitigate the asymmetry observed in these experiments.

Realigning the laser to eliminate the laser mode-one drive asymmetry was not possible during the experimental campaign because laser realignment is a time-consuming process that requires the OMEGA laser and diagnostics to be reconfigured specifically for the laser alignment. Therefore, mitigation strategies were developed that can introduce laser-drive corrections without requiring a full laser realignment.

Two techniques have been proposed for mitigating mode-one asymmetries in laser-direct-drive implosions. The first technique relies on using strategic modifications to the individual beam energies in order to redistribute the laser energy on target to apply low-mode laser-drive corrections.[45] This strategy is advantageous since the individual laser beam energies can be modified with sub-percent accuracy and can be done in such a way as to suppress multiple low modes (i.e., not just $\ell = 1$). This strategy suffers, though, in that when the full OMEGA laser energy is used, it can require some beam energies to exceed the damage threshold of the optics in the beam path and therefore requires a reduction in the total energy on target to be used. The second technique relies on using controlled target offsets to geometrically redistribute the beam overlap intensity on the target. This technique is capable of only applying mode-one laser corrections but can be used when the full laser energy of OMEGA is required. This technique has the disadvantage that it relies on accurate target placement, which, with the current target positioning system on OMEGA, is limited to ~5-μm accuracy and can be affected by random target vibrations at shot time.

Based on its simplicity and the ability to be used at the full laser energy of OMEGA, the target-offset strategy was used in these experiments. In order to determine the appropriate target offset required to mitigate the observed asymmetry, the hot-spot velocity was used to quantify the magnitude and direction of the laser mode-one drive asymmetry. The hot-spot velocity $\vec{u}_{hs}$ is assumed to have a linear relationship with the target offset $\vec{o}$ and is given by

$$\vec{u}_{hs} = \alpha\vec{o} = \alpha(\vec{r} + \vec{c}), \qquad (2)$$

where α is the offset to velocity conversion in km/s/μm, and the total offset is assumed to be the sum of the measured offset $\vec{r}$ from the high-speed video camera and some unknown effective target offset $\vec{c}$. The unknown effective target offset is the component of the hot-spot velocity generated from an assumed static mode-one asymmetry source (either laser or target) present in the system. This model is supported by both experimental data[46] and simulation results.[21]

Given at least two measurements of both the hot-spot velocity $\vec{u}_{hs}$ and high-speed video target offset $\vec{r}$, the terms α and $\vec{c}$ can be determined, through a least squares minimization. Once the vector $\vec{c}$ is determined, the hot-spot velocity, and therefore laser mode-one drive asymmetry, in an experiment can be eliminated by intentionally moving the target offset to the location $-\vec{c}$.

These calculations were performed using the experimental results from the experiments discussed above and the target was positioned to the calculated location to eliminate the observed asymmetry. The

offset to velocity conversion for these experiments was found to be 4.1 ± 0.2 km/s/μm. The unknown effective target offset was determined to be $\vec{c} = \langle -26, 33, 17 \rangle$ μm. This corresponds to a total target offset of 45 μm in the direction $\theta = 112°$ and $\phi = 308°$.

For shot 94715, the target was positioned at $\vec{r} = \langle 28, -35, -19 \rangle$ μm, which was within a few micrometers away from the requested location of $\langle 26, -33, -17 \rangle$ μm. The direction of the target offset in the OMEGA target chamber coordinate system is shown in Fig. 13. With the target positioned to this location, the asymmetry present in the previous experiments was greatly mitigated. In particular, the hot-spot velocity was reduced to 27 ± 11 km/s and was in the direction $\theta = 109° \pm 35°$ and $\phi = 341° \pm 26°$ and is shown in Fig. 13. As can be seen from Fig. 10, the apparent ion-temperature asymmetry was greatly reduced to 0.5 ± 0.5 keV. A fit to the measured apparent ion temperatures shows a slight enhancement in the minimum ion temperature to $T_0 = 4.6$ keV and the ion temperature variation being reduced to $\Delta T = 0.03$ keV. Additionally, the areal-density asymmetry shown in Fig. 11 was reduced to 37 ± 12 mg/cm^2. A fit to the measured ρR values shows little change in the average areal density $\rho R_0 = 115$ mg/cm^2 but with a greatly reduced areal-density variation $\Delta \rho R = 4$ mg/cm^2. Finally, the x-ray self-emission images became significantly more symmetric when the offset correction was applied and is shown in Fig. 14.

To understand how the target-offset correction was able to mitigate the previously observed asymmetry, it is instructive to analyze the hard sphere illumination nonuniformity for shot 94715. Figure 13 shows that when the target correction was applied, the on-target illumination uniformity was improved by a factor of 2 as compared to shot 94712 (see Fig. 8). In particular, the total illumination perturbation variation around the target was reduced to 14%. A Legendre-mode spectral decomposition of the illumination uniformity is shown in Fig. 13 and reveals that the laser-drive mode-one $\sigma_{rms}^{\ell=1}$ amplitude was reduced from 7.3% to 4.3%.
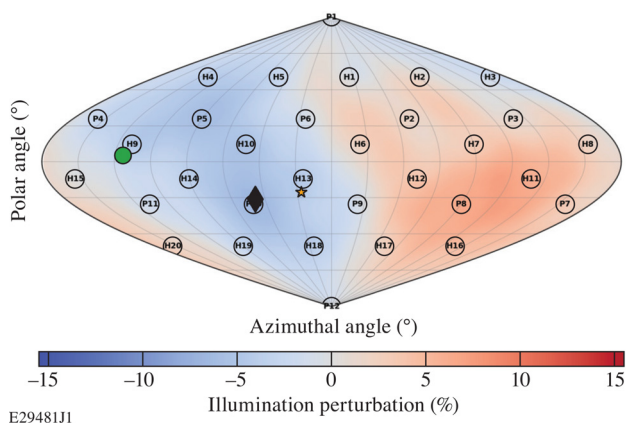

FIG. 13. A sinusoidal projection of the OMEGA target chamber showing the illumination perturbation from the mean for shot 94715 determined from a hard sphere calculation which used the measured laser beam pointing, energy, and target offset. The direction of the measured hot-spot velocity is shown as the orange star and had a magnitude of 27 km/s. The laser mode-one illumination asymmetry $\sigma_{rms}^{\ell=1}$ amplitude was 4.3% and the direction is shown as the green circle. The target-offset correction was 43 μm and is shown as the black diamond.

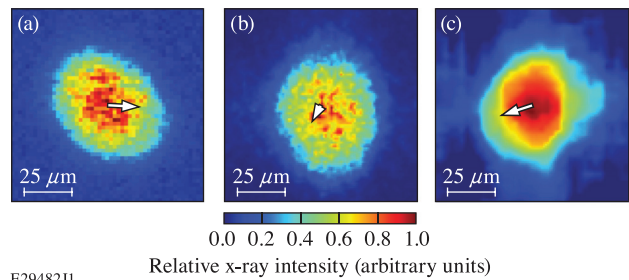FIG. 14. The x-ray self-emission images measured for shot 94715. The (a) SLOS-TRIXI[12] and (b) KB framed[11] images are time resolved and are averaged over a 40 and 15 ps time window around peak neutron production, respectively, while the (c) GMXI[11] image is time integrated. Each detector has a ∼6 μm spatial resolution. The projection of the measured hot-spot velocity into the detector plane is indicated by the white arrow. The magnitude of the projection is indicated by the length of the white arrow. The elongation observed in the x-ray images in Fig. 12 has been eliminated by applying the offset correction.

The residual drive asymmetry present in the hard sphere calculation for shot 94715 suggests that there was a slight overcorrection when applying the target-offset correction. This is consistent with the slight areal-density asymmetry still present and some residual asymmetry in the x-ray images shown in Fig. 14. With more-accurate placement of the target and repeated measurements of the hot-spot velocity, the target-offset correction can be refined to fully eliminate the observed asymmetry.

Although there is a slight residual asymmetry observed in the experiment, the illumination variation value of 14% calculated through the hard sphere calculation is an upper limit on the asymmetry that was likely present in the experiment. This is because the target offset applied on this shot was large, which can enhance the effects of laser–plasma interactions. The effects of laser–plasma interactions are not included in the hard sphere illumination calculations because they require more-complicated physics models and is an area of active research. Recent work[21] using a more-complete description of the laser illumination on target has shown that when large target offsets (∼40 μm) are present, the increase in the overlap between beams causes an enhancement in the rate at which cross-beam energy transfer (CBET) occurs. This was found to suppress the mode-one drive asymmetry and led to a reduction in the laser-drive asymmetry when compared to a hard sphere calculation.[21]

VI. EFFECT OF MODE-ONE ASYMMETRY ON IMPLOSION PERFORMANCE

The experiments described above represent a controlled set of experiments where a laser mode-one drive asymmetry was present and was then mitigated. Therefore, these experiments are good candidates to experimentally study the yield degradation due to the laser mode-one drive asymmetries in laser-direct-drive implosions. Figure 15 shows the measured DT fusion yield as a function of the hot-spot velocity for the experiments described above. We observed a 30% increase in the fusion yield for the shot (94715) where the correction was applied as compared to the shots (94657, 94660, 94712) where no correction was applied, and the mode-one asymmetry was present. It should be noted that some of the variation in the yield for
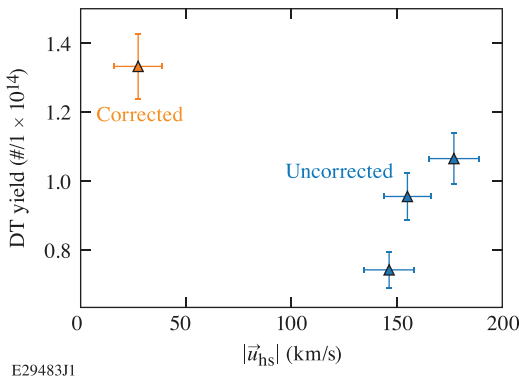
FIG. 15. The measured DT fusion yield as a function of the hot-spot velocity magnitude. The shot with the asymmetry correction applied (94715) is shown in orange, while the three shots (94657, 94660, 94712) where no correction was applied are shown in blue. We see that suppressing the laser mode-one drive asymmetry leads to a 30% average increase in the fusion yield compared to the uncorrected shots.

FIG. 16. The pressure degradation from 1D as a function of the parameter $f = |\vec{u}_{hs}|/u_{imp,LILAC}$. Shown is a fit using the functional form suggested in Ref. 49 and the analytic result using a piston model.[49] Note that the scatter in the data are likely due to the presence of other asymmetries that the hot-spot velocity does not capture.

the uncorrected shots is due to age of the DT fuel used in these experiments being different.[47]

The exact fusion yield on any given experiment is a complicated expression that has several dependencies such as the exact 3D mode asymmetry in the experiment, the fill age, the laser spot size, the target offset, and other terms, which are still being identified. This complicates a direct comparison between the fusion yield and the hot-spot velocity across a broad ensemble of shots. Therefore, it is useful to study the effect that mode-one asymmetries have on a hydrodynamic quantity such as the hot-spot pressure, which incorporates several of the hydrodynamic properties of the implosion into a single value.

Figure 16 shows the ratio of the experimentally inferred hot-spot pressure to the pressure predicted from post-shot simulations using the 1D radiation-hydrodynamic code $LILAC$[48] as a function of the mode-one asymmetry parameter f. The mode-one asymmetry parameter[49] is defined as the ratio of the experimentally inferred hot-spot velocity to the peak implosion velocity from the post-shot $LILAC$ simulation. The experimental hot-spot pressure has been inferred by assuming an isobaric hot-spot density and temperature profile[50] and fitting the profile to match the inferred fusion yield and minimum apparent ion temperature given the measurements of the hot-spot radius and burn width.[51] The data shown in Fig. 16 are from 48 cryogenic LDD experiments performed on OMEGA since 2019 and used a variety of laser pulse and target designs.

From Fig. 16, we see that the hot-spot pressure degradation tends to increase with the mode-one asymmetry parameter, and that the OMEGA data lie below the prediction from an analytic piston model.[49] The analytic piston model only considers the presence of a pure mode-one drive asymmetry and assumes a simplified implosion geometry, and therefore provides an upper bound for the pressure degradation expected in an experiment. A fit to the OMEGA data using the model $P_{exp}/P_{1-D} = (1 - f^2)^n$ as suggested in Ref. 49 is shown in Fig. 16. The best-fit value for the exponent parameter n was found to be $n = 11 \pm 1$ with a reduced chi-squared of 4.5 and suggests that a more sophisticated model is required to explain the data. This is plausible as there may exist other low- or high-mode asymmetries in these implosions, which are not described by the model.
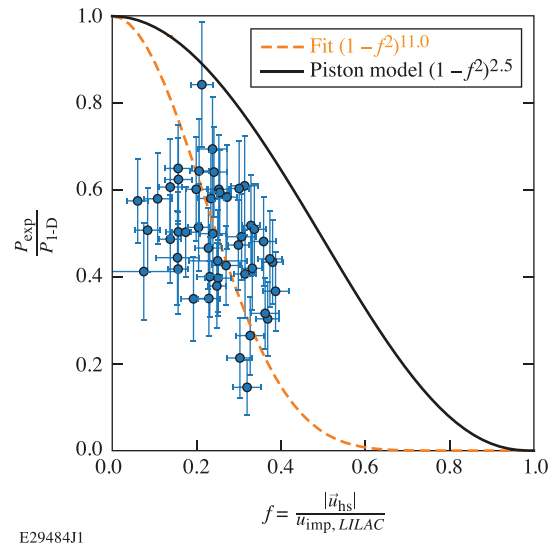
Understanding the trend observed in Fig. 16 will be the focus of future work.

VII. CONCLUSIONS

Here, we have demonstrated how mode-one drive asymmetries have been diagnosed in cryogenic DT laser-direct-drive implosions on OMEGA using the suite of nuclear and x-ray diagnostics that have been developed. We find that when large laser mode-one drive asymmetries exist, large hot-spot velocities (>100 km/s) are observed in the direction of the laser-drive asymmetry. Additionally, we saw that the direction and magnitude of the apparent ion temperature and areal-density asymmetry were aligned with the hot-spot velocity direction. Finally, 3D hot-spot x-ray images revealed that the elongation observed in these images was aligned with the hot-spot velocity measurements.

A new asymmetry mitigation technique was demonstrated that uses the measured hot-spot velocity to determine the optimal target position to minimize mode-one asymmetries. This technique enables corrections to be applied in laser-direct-drive implosions that require the full laser energy of OMEGA to be used and can be applied without realigning the laser system. This technique was successfully demonstrated and a more-symmetric hot spot with a greatly reduced hot-spot velocity, apparent ion-temperature asymmetry, and areal-density asymmetry was observed. It was shown that with the laser mode-one drive asymmetry mitigated, the fusion yield was increased by ∼30%. We have also presented the first experimental data on the relationship between the reduction in the hot-spot pressure due to mode-one drive asymmetries in laser-direct-drive implosions.

These results highlight the importance of accurate beam alignment in laser-direct-drive implosions and the importance of nuclear and x-ray diagnostics in ICF research. Motivated by these results,

improvements to both the laser alignment analysis routines and the targets used during laser alignment have been made. These improvements have resulted in laser mode-one drive asymmetries on OMEGA being routinely <2% as is shown in Fig. 9. Future work will focus on reducing laser mode-one drive asymmetries to <1% by increasing the number of pinhole cameras used during the beam-pointing experiments, and to increase the number of beam-pointing experiments. Finally, 3D reconstructions of the hot spot and fuel conditions using measurements made by the suite of nuclear and x-ray diagnostics on OMEGA are being developed and will provide new insights into multidimensional effects in laser-direct drive implosions.[44]

DATA AVAILABILITY

The data that support the findings of this study are available from the corresponding author upon reasonable request.

REFERENCES

[1] J. Nuckolls, L. Wood, A. Thiessen, and G. Zimmerman, Nature **239**, 139 (1972).
[2] A. F. Gibson, Phys. Educ. **15**, 4 (1980).
[3] A. R. Christopherson, R. Betti, S. Miller, V. Gopalaswamy, O. M. Mannion, and D. Cao, Phys. Plasmas **27**, 052708 (2020).
[4] E. I. Moses, R. N. Boyd, B. A. Remington, C. J. Keane, and R. Al-Ayat, Phys. Plasmas **16**, 041006 (2009).
[5] T. R. Boehly, D. L. Brown, R. S. Craxton, R. L. Keck, J. P. Knauer, J. H. Kelly, T. J. Kessler, S. A. Kumpan, S. J. Loucks, S. A. Letzring, F. J. Marshall, R. L. McCrory, S. F. Morse, W. Seka, J. M. Soures, and C. P. Verdon, Opt. Commun. **133**, 495 (1997).
[6] B. K. Spears, M. J. Edwards, S. Hatchett, J. Kilkenny, J. Knauer, A. Kritcher, J. Lindl, D. Munro, P. Patel, H. F. Robey, and R. P. J. Town, Phys. Plasmas **21**, 042702 (2014).
[7] K. M. Woo, R. Betti, D. Shvarts, O. M. Mannion, D. Patel, V. N. Goncharov, K. S. Anderson, P. B. Radha, J. P. Knauer, A. Bose, V. Gopalaswamy, A. R. Christopherson, E. M. Campbell, J. Sanz, and H. Aluie, Phys. Plasmas **25**, 102710 (2018).
[8] H. G. Rinderknecht, D. T. Casey, R. Hatarik, R. M. Bionta, B. J. MacGowan, P. Patel, O. L. Landen, E. P. Hartouni, and O. A. Hurricane, Phys. Rev. Lett. **124**, 145002 (2020).
[9] D. T. Casey, B. J. Macgowan, J. D. Sater, A. B. Zylstra, O. L. Landen, J. Milovich, O. A. Hurricane, A. L. Kritcher, M. Hohenberger, K. Baker, S. L. Pape, T. Döppner, C. Weber, H. Huang, C. Kong, J. Biener, C. V. Young, S. Haan, R. C. Nora, S. Ross, H. Robey, M. Stadermann, A. Nikroo, D. A. Callahan, R. M. Bionta, K. D. Hahn, A. S. Moore, D. Schlossberg, M. Bruhn, K. Sequoia, N. Rice, M. Farrell, and C. Wild, Phys. Rev. Lett. **126**, 25002 (2021).
[10] O. M. Mannion, J. P. Knauer, V. Yu. Glebov, C. J. Forrest, A. Liu, Z. L. Mohamed, M. H. Romanofsky, T. C. Sangster, C. Stoeckl, and S. P. Regan, Nucl. Instrum. Methods Phys. Res., Sect. A **964**, 163774 (2020).
[11] F. J. Marshall, R. E. Bahr, V. N. Goncharov, V. Yu. Glebov, B. Peng, S. P. Regan, T. C. Sangster, and C. Stoeckl, Rev. Sci. Instrum. **88**, 093702 (2017).
[12] W. Theobald, C. Sorce, M. Bedzyk, S. T. Ivancic, F. J. Marshall, C. Stoeckl, R. C. Shah, M. Lawrie, S. P. Regan, T. C. Sangster, E. M. Campbell, T. Hilsabeck, K. Englehorn, J. D. Kilkenny, D. Morris, M. Chung, J. D. Hares, A. K. L. Dymoke-Bradshaw, P. Bell, J. Celeste, A. C. Carpenter, M. Dayton, D. K. Bradley, M. C. Jackson, L. Pickworth, S. Nagel, G. Rochau, J. Porter, M. Sanchez, L. Claus, G. Robertson, and Q. Looker, Rev. Sci. Instrum. **89**, 10G117 (2018).
[13] R. Hatarik, D. B. Sayre, J. A. Caggiano, T. Phillips, M. J. Eckart, E. J. Bond, C. J. Cerjan, G. P. Grim, E. P. Hartouni, J. P. Knauer, J. M. Mcnaney, and D. H. Munro, J. Appl. Phys. **118**, 184502 (2015).
[14] C. J. Forrest, P. B. Radha, V. Yu. Glebov, V. N. Goncharov, J. P. Knauer, A. Pruyne, M. Romanofsky, T. C. Sangster, M. J. Shoup III, C. Stoeckl, D. T. Casey, M. Gatu-Johnson, and S. Gardner, Rev. Sci. Instrum. **83**, 10D919 (2012).
[15] M. Gatu Johnson, J. P. Knauer, C. J. Cerjan, M. J. Eckart, G. P. Grim, E. P. Hartouni, R. Hatarik, J. D. Kilkenny, D. H. Munro, D. B. Sayre, B. K. Spears, R. M. Bionta, E. J. Bond, J. A. Caggiano, D. Callahan, D. T. Casey, T. Döppner, J. A. Frenje, V. Y. Glebov, O. Hurricane, A. Kritcher, S. LePape, T. Ma, A. Mackinnon, N. Meezan, P. Patel, R. D. Petrasso, J. E. Ralph, P. T. Springer, and C. B. Yeamans, Phys. Rev. E **94**, 021202(R) (2016).
[16] J. J. Ruby, A. Pak, J. E. Field, T. Ma, B. K. Spears, L. R. Benedetti, D. K. Bradley, L. F. Berzak Hopkins, D. T. Casey, T. Döppner, D. Eder, D. Fittinghoff, G. Grim, R. Hatarik, D. E. Hinkel, N. Izumi, J. D. Kilkenny, S. F. Khan, J. P. Knauer, A. L. Kritcher, F. E. Merrill, J. D. Moody, S. R. Nagel, H.-S. Park, J. D. Salmonson, D. B. Sayre, D. A. Callahan, W. W. Hsing, O. A. Hurricane, P. K. Patel, and M. J. Edwards, Phys. Plasmas **23**, 072701 (2016).
[17] I. V. Igumenshchev, V. N. Goncharov, F. J. Marshall, J. P. Knauer, E. M. Campbell, C. J. Forrest, D. H. Froula, V. Y. Glebov, R. L. McCrory, S. P. Regan, T. C. Sangster, S. Skupsky, and C. Stoeckl, Phys. Plasmas **23**, 052702 (2016).
[18] I. V. Igumenshchev, D. T. Michel, R. C. Shah, E. M. Campbell, R. Epstein, C. J. Forrest, V. Yu. Glebov, V. N. Goncharov, J. P. Knauer, F. J. Marshall, R. L. McCrory, S. P. Regan, T. C. Sangster, C. Stoeckl, A. J. Schmitt, and S. Obenschain, Phys. Plasmas **24**, 056307 (2017).
[19] A. L. Kritcher, R. Town, D. Bradley, D. Clark, B. Spears, O. Jones, S. Haan, P. T. Springer, J. Lindl, R. H. H. Scott, D. Callahan, M. J. Edwards, and O. L. Landen, Phys. Plasmas **21**, 042708 (2014).
[20] J. A. Marozas, M. Hohenberger, M. J. Rosenberg, D. Turnbull, T. J. Collins, P. B. Radha, P. W. McKenty, J. D. Zuegel, F. J. Marshall, S. P. Regan, T. C. Sangster, W. Seka, E. M. Campbell, V. N. Goncharov, M. W. Bowers, J. M. Di Nicola, G. Erbert, B. J. MacGowan, L. J. Pelz, and S. T. Yang, Phys. Rev. Lett. **120**, 85001 (2018).
[21] K. S. Anderson, C. J. Forrest, O. M. Mannion, F. J. Marshall, R. C. Shah, D. T. Michel, J. A. Marozas, P. B. Radha, D. H. Edgell, R. Epstein, V. N. Goncharov, J. P. Knauer, M. Gatu Johnson, and S. Laffite, Phys. Plasmas **27**, 112713 (2020).
[22] F. Weilacher, P. B. Radha, and C. Forrest, Phys. Plasmas **25**, 042704 (2018).
[23] H. Brysk, Plasma Phys. **15**, 611 (1973).
[24] T. J. Murphy, Phys. Plasmas **21**, 072701 (2014).
[25] A. J. Crilly, B. D. Appelbe, O. M. Mannion, C. J. Forrest, V. Gopalaswamy, C. A. Walsh, and J. P. Chittenden, Phys. Plasmas **27**, 012701 (2020).
[26] A. J. Crilly, B. D. Appelbe, O. M. Mannion, C. J. Forrest, and J. P. Chittenden, "The effect of areal density asymmetries on scattered neutron spectra in ICF implosions," Phys. Plasmas **28**, 022710 (2021).
[27] C. J. Forrest, A. Deltuva, W. U. Schröder, A. V. Voinov, J. P. Knauer, E. M. Campbell, G. W. Collins, V. Y. Glebov, O. M. Mannion, Z. L. Mohamed, P. B.

Radha, S. P. Regan, T. C. Sangster, and C. Stoeckl, Phys. Rev. C **100**, 034001 (2019).

[28] L. Ballabio, J. Källne, and G. Gorini, Nucl. Fusion **38**, 1723 (1998).

[29] B. Appelbe and J. Chittenden, Plasma Phys. Controlled Fusion **53**, 045002 (2011).

[30] T. J. Murphy, R. E. Chrien, and K. A. Klare, Rev. Sci. Instrum. **68**, 614 (1997).

[31] A. J. Crilly, B. D. Appelbe, K. McGlinchey, C. A. Walsh, J. K. Tong, A. B. Boxall, and J. P. Chittenden, Phys. Plasmas **25**, 122703 (2018).

[32] R. A. Lerche, L. W. Coleman, J. W. Houghton, D. R. Speck, and E. K. Storm, Appl. Phys. Lett. **31**, 645 (1977).

[33] D. T. Casey, J. A. Frenje, M. Gatu Johnson, F. H. Séguin, C. K. Li, R. D. Petrasso, V. Yu. Glebov, J. Katz, J. Magoon, D. D. Meyerhofer, T. C. Sangster, M. Shoup, J. Ulreich, R. C. Ashabranner, R. M. Bionta, A. C. Carpenter, B. Felker, H. Y. Khater, S. Lepape, A. Mackinnon, M. A. McKernan, M. Moran, J. R. Rygg, M. F. Yeoman, R. Zacharias, R. J. Leeper, K. Fletcher, M. Farrell, D. Jasion, J. Kilkenny, and R. Paguio, Rev. Sci. Instrum. **84**, 043506 (2013).

[34] M. G. Johnson, J. A. Frenje, D. T. Casey, C. K. Li, F. H. Séguin, R. Petrasso, R. Ashabranner, R. M. Bionta, D. L. Bleuel, E. J. Bond, J. A. Caggiano, A. Carpenter, C. J. Cerjan, T. J. Clancy, T. Doeppner, M. J. Eckart, M. J. Edwards, S. Friedrich, S. H. Glenzer, S. W. Haan, E. P. Hartouni, R. Hatarik, S. P. Hatchett, O. S. Jones, G. Kyrala, S. Le Pape, R. A. Lerche, O. L. Landen, T. Ma, A. J. MacKinnon, M. A. McKernan, M. J. Moran, E. Moses, D. H. Munro, J. McNaney, H. S. Park, J. Ralph, B. Remington, J. R. Rygg, S. M. Sepke, V. Smalyuk, B. Spears, P. T. Springer, C. B. Yeamans, M. Farrell, D. Jasion, J. D. Kilkenny, A. Nikroo, R. Paguio, J. P. Knauer, V. Yu. Glebov, T. C. Sangster, R. Betti, C. Stoeckl, J. Magoon, M. J. Shoup, G. P. Grim, J. Kline, G. L. Morgan, T. J. Murphy, R. J. Leeper, C. L. Ruiz, G. W. Cooper, and A. J. Nelson, Rev. Sci. Instrum. **83**, 10D308 (2012).

[35] A. Bose, R. Betti, D. Shvarts, and K. M. Woo, Phys. Plasmas **24**, 102704 (2017).

[36] R. A. Lerche and B. A. Remington, Rev. Sci. Instrum. **61**, 3131 (1990).

[37] R. A. Lerche, D. R. Kania, S. M. Lane, G. L. Tietbohl, C. K. Bennett, and G. P. Baltzer, Rev. Sci. Instrum. **59**, 1697 (1988).

[38] R. Hatarik, R. C. Nora, B. K. Spears, M. J. Eckart, G. P. Grim, E. P. Hartouni, A. S. Moore, and D. J. Schlossberg, Rev. Sci. Instrum. **89**, 10I138 (2018).

[39] O. M. Mannion, V. Yu. Glebov, C. J. Forrest, J. P. Knauer, V. N. Goncharov, S. P. Regan, T. C. Sangster, C. Stoeckl, and M. Gatu Johnson, Rev. Sci. Instrum. **89**, 10I131 (2018).

[40] V. Yu. Glebov, C. J. Forrest, K. L. Marshall, M. Romanofsky, T. C. Sangster, M. J. Shoup III, and C. Stoeckl, Rev. Sci. Instrum. **85**, 11E102 (2014).

[41] F. J. Marshall, J. A. Delettrez, R. Epstein, R. Forties, R. L. Keck, J. H. Kelly, P. W. McKenty, S. P. Regan, and L. J. Waxer, Phys. Plasmas **11**, 251 (2004).

[42] R. A. Forties and F. J. Marshall, Rev. Sci. Instrum. **76**, 073505 (2005).

[43] W. Grimble, F. J. Marshall, and E. Lambrides, Phys. Plasmas **25**, 072702 (2018).

[44] O. M. Mannion, K. M. Woo, A. J. Crilly, C. J. Forrest, J. A. Frenje, M. G. Johnson, V. Y. Glebov, J. P. Knauer, Z. L. Mohamed, M. H. Romanofsky, C. Stoeckl, W. Theobald, and S. P. Regan, Rev. Sci. Instrum. Phys. Plasmas **92**, 033529 (2021).

[45] D. T. Michel, I. V. Igumenshchev, A. K. Davis, D. H. Edgell, D. H. Froula, D. W. Jacobs-Perkins, V. N. Goncharov, S. P. Regan, A. Shvydky, and E. M. Campbell, Phys. Rev. Lett. **120**, 125001 (2018).

[46] M. Gatu Johnson, P. J. Adrian, K. S. Anderson, B. D. Appelbe, J. P. Chittenden, A. J. Crilly, D. Edgell, C. J. Forrest, J. A. Frenje, V. Yu. Glebov, B. M. Haines, I. Igumenshchev, D. Jacobs-Perkins, R. Janezic, N. V. Kabadi, J. P. Knauer, B. Lahmann, O. M. Mannion, F. J. Marshall, T. Michel, F. H. Séguin, R. Shah, C. Stoeckl, C. A. Walsh, and R. D. Petrasso, Phys. Plasmas **27**, 032704 (2020).

[47] A. Lees, R. Betti, J. P. Knauer, V. Gopalaswamy, D. Patel, R. Epstein, J. Carroll-Nellenback, A. R. Christopherson, K. M. Woo, O. M. Mannion, Z. L. Mohamed, F. J. Marshall, C. Stoeckl, V. Yu. Glebov, S. P. Regan, R. C. Shah, D. H. Edgell, D. Coa, V. N. Goncharov, I. V. Igumenshchev, P. B. Radha, T. J. B. Collins, T. C. Sangster, E. M. Campbell, M. Gatu Johnson, R. D. Petrasso, C. K. Li, and J. A. Frenje, "Understanding the fusion yield and all of its dependencies using statistical modeling of experimental data," paper presented at the 62nd Annual Meeting of the American Physical Society Division of Plasmas Physics, Memphis, TN, 9–13 November 2020.

[48] J. Delettrez, R. Epstein, M. C. Richardson, P. A. Jaanimagi, and B. L. Henke, Phys. Rev. A **36**, 3926 (1987).

[49] O. A. Hurricane, D. T. Casey, O. Landen, A. L. Kritcher, R. Nora, P. K. Patel, J. A. Gaffney, K. D. Humbird, J. E. Field, M. K. G. Kruse, J. L. Peterson, and B. K. Spears, Phys. Plasmas **27**, 062704 (2020).

[50] R. Betti, M. Umansky, V. Lobatchev, V. N. Goncharov, and R. L. McCrory, Phys. Plasmas **8**, 5257 (2001).

[51] S. P. Regan, V. N. Goncharov, I. V. Igumenshchev, T. C. Sangster, R. Betti, A. Bose, T. R. Boehly, M. J. Bonino, E. M. Campbell, D. Cao, T. J. Collins, R. S. Craxton, A. K. Davis, J. A. Delettrez, D. H. Edgell, R. Epstein, C. J. Forrest, J. A. Frenje, D. H. Froula, M. Gatu Johnson, V. Yu. Glebov, D. R. Harding, M. Hohenberger, S. X. Hu, D. Jacobs-Perkins, R. Janezic, M. Karasik, R. L. Keck, J. H. Kelly, T. J. Kessler, J. P. Knauer, T. Z. Kosc, S. J. Loucks, J. A. Marozas, F. J. Marshall, R. L. McCrory, P. W. McKenty, D. D. Meyerhofer, D. T. Michel, J. F. Myatt, S. P. Obenschain, R. D. Petrasso, P. B. Radha, B. Rice, M. J. Rosenberg, A. J. Schmitt, M. J. Schmitt, W. Seka, W. T. Shmayda, M. J. Shoup III, A. Shvydky, S. Skupsky, A. A. Solodov, C. Stoeckl, W. Theobald, J. Ulreich, M. D. Wittman, K. M. Woo, B. Yaakobi, and J. D. Zuegel, Phys. Rev. Lett. **117**, 025001 (2016).